



A Dynamic Trajectory Fit to Multisensor Fireball Observations

Trent Jansen-Sturgeon , Eleanor K. Sansom , Hadrien A. R. Devillepoix , Philip A. Bland , Martin C. Towner ,
Robert M. Howie , and Benjamin A. D. Hartig 

School of Earth and Planetary Sciences, Curtin University, GPO Box U1987, Perth, WA 6845, Australia
Received 2019 October 31; revised 2020 August 15; accepted 2020 August 17; published 2020 September 30

Abstract

Meteorites with known orbital origins are key to our understanding of solar system formation and the source of life on Earth. Fireball networks have been developed globally in a unified effort to record and ultimately retrieve these cosmic samples. However, the accuracy of the determined orbit and the likelihood of meteorite recovery depend directly on the accuracy of the chosen meteoroid triangulation method. There are three leading techniques for meteoroid triangulation discussed in the literature: the method of planes, the straight-line least-squares method, and the multiparameter fit method. Here we describe an alternative method to meteoroid triangulation, called the dynamic trajectory fit. This approach uses the meteoroid's 3D dynamic equations of motion to fit a realistic trajectory directly to multisensor line-of-sight observations. This method has the ability to resolve fragmentation events, fit systematic observatory timing offsets, and determine mass estimates of the meteoroid along its observable trajectory. Through a comprehensive Monte Carlo analysis of over 100,000 trajectory simulations, we find this new method to more accurately estimate meteoroid trajectories of slow entry events ($<25 \text{ km s}^{-1}$) and events observed from low convergence angles ($<10^\circ$) compared to existing meteoroid triangulation techniques. Additionally, we triangulate an observed fireball event with visible fragmentation using the various triangulation methods to show that the proposed dynamic trajectory fit implementing fragmentation to best match the captured multisensor line-of-sight data.

Unified Astronomy Thesaurus concepts: [Meteoroids \(1040\)](#); [Fireballs \(538\)](#)

1. Introduction

Fireball networks have been around since the 1960s, with the specific goal of observing meteors from multiple stations to determine their past and future trajectories (Ceplecha 1961). The meteoroids of real interest are the bright, deeply penetrating kind, with the highest chance of surviving the violent atmospheric entry process to produce meteorites. Finding meteorites with known orbits is key for giving these cosmic samples a regional context in the greater solar system, potentially helping to answer some of the biggest questions in planetary science, such as solar system formation and the origin of life on Earth. However, these pristine samples of space material are incredibly rare. As of mid-2019, only 36 out of about 60,000 collected meteorites have known orbits, 5 of which have been found in recent history by the Global Fireball Observatory (GFO), a global collaboration of fireball networks, including Australia's Desert Fireball Network (DFN).

Successful recovery of the incoming meteorite requires accurate knowledge of the fall position. If found, it is highly desirable to have a well-constrained and accurate orbit associated with the sample. Determining an orbit requires the entry radiant and velocity of the meteoroid, while the prediction of fall positions require dark-flight modeling, where dark flight is the period of meteoroid freefall to Earth after visible observations cease, during which the body is strongly influenced by its size and shape, as well as atmospheric winds. At the heart of all these dynamic analyses lies the triangulation and modeling of the observed luminous trajectory, giving both the dark flight and orbit determination their initial conditions. To improve the accuracy of these predictions, we must first improve the accuracy of our triangulation modeling techniques.

Three prominent methods of meteoroid triangulation have been documented and used in the past: method of planes

(MOP; Ceplecha 1987), straight-line least squares (SLLS; Borovicka 1990), and multiparameter fit (MPF; Gural 2012). These three methods are outlined conceptually below. For more details and mathematical rigor, please refer to their respective papers.

A notable additional technique is the particle filter modeling method of Sansom et al. (2019) as an alternative to the traditional triangulation methods. While particle-type approaches are thorough, they are also quite computationally intense and are not feasible as the default triangulation method for large meteoroid data sets. Instead, it is generally best suited to special cases when a surviving meteorite is suspected.

1.1. Method of Planes (Ceplecha 1987)

Although the MOP is the oldest and least accurate of the three prominent triangulation methods, it is very computationally simple and often used for constructing the initial trajectory guess for more complex methods, such as the SLLS and MPF (see Sections 1.2 and 1.3). MOP comprises four main steps: plane construction, radiant formation, position determination, and velocity fitting.

To begin, MOP constructs a plane for every sensor. This plane includes the sensor's location and best fits to its associated observation rays using a least-squares approach. It does so by adjusting the plane normal to minimize the square of the angular residuals between the rays and the plane.

Once the optimum plane is calculated for each sensor, they are intersected in 3D space to determine the straight-line trajectory. In the case where more than two sensors recorded the meteoroid, a statistical weighting can be used to combine the straight-line solutions from every different sensor-pair combination to produce one unique straight-line trajectory. This weighting is based on the convergence angle between the

two planes as well as on the combined angular span of the observed meteoroid across the sensors.

Positions along the determined straight-line trajectory are found for every observation (regardless of time) as the closest point on the trajectory line from that observed line of sight. These 3D positions are generally calculated by the intersection of the trajectory itself with a series of planes that each contain an individual line of sight and its associated optimum plane normal.

Lastly, the velocities are determined by fitting a model to the positional lengths along the trajectory as a function of time. These velocity models and fitting methods are described by Pecina & Ceplecha (1983, 1984). However, it is interesting to note that Pecina & Ceplecha (1983, 1984) state these equations are “violated” for longer trajectories, indicating the simplicity of their chosen velocity models.

1.2. Straight Line Least Squares (Borovicka 1990)

Only three years after MOP, the SLLS method was published. Although Borovicka (1990) showed that the SLLS method produced lower residuals than MOP, they concluded that both methods produce similar results and could not recommend one over the other, even suggesting a combination of both may be preferable, depending on the case. That said, Gural (2012) found the SLLS method to be more robust when lower resolution cameras were used.

Unlike MOP, the SLLS method best fits a straight-line trajectory directly to all the observed lines of sight at once. It does so by minimizing the perpendicular distances between the lines of sight and the straight-line trajectory itself. It was later stated by Gural (2012) that a better alternative to the initially published SLLS method was to minimize the angular distance rather than the perpendicular distance. Using the angular distance acts to indirectly weight the line-of-sight measurements based on their observation range.

The positions are determined for every line of sight by determining the closest point on the optimized straight-line trajectory to that given line of sight (regardless of time). Similar to MOP, the SLLS method requires a separate step to determine the velocity along the trajectory. The methods of Pecina & Ceplecha (1983, 1984) are used to determine this velocity by considering the 1D lengths along the trajectory over time.

We must note that Borovicka (1990) offers the SLLS method in both the Earth-centered/Earth-fixed (ECEF) frame and the Earth-centered Inertial (ECI) frame; the main difference is where the straight-line trajectory is defined. Performing the SLLS method in the ECI frame implicitly includes the Coriolis force but requires absolute timing knowledge to operate. It is up to the user to determine which variation is more physically realistic.

1.3. Multiparameter Fit (Gural 2012)

The previously discussed MOP and SLLS methods are purely geometric triangulation solutions, i.e., the trajectory-fitting component can be performed without any timing information. It is only as a second step, when velocity analysis is needed, that timing of the observed meteoroid is considered. This means MOP and SLLS determine a unique position for every line of sight; if there are simultaneous observations from N sensors, there will be N unique positions along the trajectory

corresponding to the same point in time. Only later, in the velocity analysis step, can this potential scatter be dealt with.

The MPF technique of Gural (2012) differs from the previous two triangulation methods in that it fits raw observations directly to a trajectory solution, combining the straight-line fitting and velocity modeling steps into one. Hence, N simultaneous observations will now result in one unique position along the trajectory. One implication of this approach is that the convergence angle can now be thought of as the angle between simultaneous lines of sight rather than between planes, which is a significant distinction.

As the name suggests, the MPF algorithm best fits unknown trajectory parameters to the measured lines of sight by minimizing the angular distance between the said lines of sight and the predicted lines of sight given their modeled positions along a straight-line trajectory. These fitting parameters include the initial position (\mathbf{p}_0), the initial velocity (\mathbf{v}_0), some deceleration coefficients depending on the chosen model (a_i), and sensor timing offsets (Δt_k), giving the MPF the ability to handle asynchronous sensors assuming they all have relative timing. Positions along the straight-line trajectory are determined using one of three velocity models: a constant velocity along the track, a linearly decreasing velocity with time, or an exponentially dependent deceleration (Jacchia et al. 1967). However, these suggested velocity models do not physically represent the trajectory dynamics. Gural (2012) suggests that this technique is most applicable to smaller mass meteors (<5 g) of short duration (<3 s), unless a better model is used.

2. New Approach—Dynamic Trajectory Fit (DTF)

Of the three most prevalent triangulation methods (as discussed in Section 1), none claim to be able to fit long-duration fireballs of significant mass, in part because all methods have assumed a straight-line trajectory. While Jenniskens (2006) claim that masses <50 g or equivalent magnitude of -2 can be approximated using straight-line trajectories, if the goal is to observe deeply penetrating fireballs such as those targeted by the GFO, the fireballs are not guaranteed to follow this straight-line assumption. In fact, Sansom et al. (2019) show that the straight-line assumption is an oversimplification that will affect orbit calculations and meteorite search regions for a significant number of fireball events.

The DTF method proposed here removes this straight-line assumption by fitting differential equations of motion directly to the measured lines of sight, thereby including all spatial/temporal information in one step and ultimately providing a more realistic account of the meteoroid’s fall trajectory. This methodology takes the ideas of global fitting proposed in Gural (2012) several steps further. The differential equations that describe meteoroid fall dynamics and ablation following Sansom et al. (2019) are¹

$$\frac{d\mathbf{v}}{dt} = -\frac{c_d A \rho_a \|\mathbf{v}_{\text{rel}}\|}{2\rho_m^{2/3} m^{1/3}} \mathbf{v}_{\text{rel}} + \mathbf{a}_{\text{grav}}, \quad (1)$$

$$\frac{dm}{dt} = -\frac{c_h A \rho_a m^{2/3} \|\mathbf{v}_{\text{rel}}\|^3}{2H^* \rho_m^{2/3}}, \quad (2)$$

¹ Assuming that the meteoroid spins rapidly enough to cause uniform ablation over its entire surface area, i.e., the shape change parameter $\mu = 2/3$ (Bronshten 1983).

where \mathbf{v} is the meteoroid’s absolute velocity in the ECI frame, \mathbf{v}_{rel} is the meteoroid’s velocity relative to the atmosphere, m is the meteoroid’s mass, \mathbf{a}_{grav} is the acceleration due to gravity,² c_d is the drag coefficient, A is the shape-density parameter (Bronshen 1983), ρ_m is the meteoroid’s density, ρ_a is the atmospheric air density,³ c_h is the heat-transfer coefficient, and H^* is the enthalpy of sublimation.

However, not every unknown parameter from Equations (1) and (2) can be resolved as many terms are dynamically coupled and therefore indistinguishable given only the line-of-sight measurements we obtain. Therefore, by assuming c_d , A , and ρ_m are constant throughout the luminous phase, we can alter these equations by grouping the coupled terms together as shown:

$$\frac{d\mathbf{v}}{dt} = -\frac{\rho_a \|\mathbf{v}_{\text{rel}}\|}{2B} \mathbf{v}_{\text{rel}} + \mathbf{a}_{\text{grav}}, \quad (3)$$

$$\frac{dB}{dt} = -\frac{\sigma \rho_a \|\mathbf{v}_{\text{rel}}\|^3}{6}, \quad (4)$$

where $B = \sqrt[3]{m\rho_m^2} / (c_d A) = m / (c_d S)$ is the meteoroid’s ballistic coefficient,⁴ $\sigma = c_h / (c_d H^*)$ is the meteoroid’s ablation coefficient, $\mathbf{v}_{\text{rel}} = \mathbf{v} - \mathbf{v}_{\text{atm}}$ is the meteoroid’s velocity relative to the atmosphere, $\mathbf{v}_{\text{atm}} = \boldsymbol{\omega}_e \times \mathbf{p}$ is the velocity of the atmosphere, $\boldsymbol{\omega}_e$ is Earth’s rotational angular velocity, \mathbf{p} is the meteoroid’s position in the ECI frame, and S is the meteoroid’s cross-sectional area.

In addition to estimating the dynamic parameters (\mathbf{p} and \mathbf{v}), by fitting the above differential equations to the measurements, the DTF method can also estimate some physical parameters, including the ballistic parameter, B , and ablation coefficient, σ . This fitted ballistic parameter, B , can be used to estimate the meteoroid’s mass⁵ during its observed descent through the atmosphere—see Section 2.1 for details.

Although some fireball networks have submillisecond timing precision on their shutter actuations within a long-exposure image, such as those observatories within the GFO (Howie et al. 2017b), the identification of the exact shutter breaks is sometimes impossible due to haloing and/or saturation of the fireball, causing the loss of all time information. Provided at least one sensor has absolute timing for reference, the DTF method is able to handle observations without timing altogether. Additionally, the DTF method can resolve any timing offsets between sensors, which is necessary for those meteor and fireball networks that only record relative time information.

One extra feature available as a consequence of the DTF approach is the option to include fragmentation events, which can be user diagnosed by large flares in the light curve. If prompted, the DTF method can resolve both time and amount of discrete fragmentation using the deceleration characteristics of the meteoroid inherent in the observations.

² Care must be taken in calculating the direction of Earth’s gravitation vector. It should be perpendicular to Earth’s ellipsoid rather than toward Earth’s center of mass—a subtle, but accumulative, difference.

³ The atmospheric density, ρ_a , is calculated using the NRLMSISE-00 empirical atmospheric model (Picone et al. 2002).

⁴ We refer to the ballistic coefficient as defined within the ballistics community. We acknowledge that there is a separate dimensionless ballistic coefficient, α , defined and used within the meteoritic community (Gritsevich 2009).

⁵ Assuming the meteoroid’s drag coefficient, c_d , shape, A , and density, ρ_m , are constant throughout its luminous trajectory.

2.1. Procedure

A mostly conceptual overview of the DTF methodology will be presented here, containing sufficient detail and references to ensure reproducibility. This conceptual overview is supplemented with a pseudocode representation of the algorithm to visually demonstrate the overall structure and information flow within the DTF method, shown in Figure 1. Additionally, all of the associated Python source code files are publicly available on the DFN’s GitHub page⁶ for reference and/or use.

Computationally, the DTF algorithm is divided into three main parts: state approximation, sanity checks, and optimization.

Part 1: State Approximation. In preparation for the main optimization step (Part 3), we must estimate all the unknown parameters for a single point in time that describe the meteoroid’s dynamics; see Equations (3) and (4). The collection of these parameters is termed the meteoroid’s “state” and is given by the following vector:

$$\mathbf{x}_{\text{est}}^f = [p_x^f, p_y^f, p_z^f, v_x^f, v_y^f, v_z^f, B^f, \sigma, \delta_{\text{frag},i}, t_{\text{frag},i}, \Delta t_j, t_k^{\text{rel}}], \quad (5)$$

where $\mathbf{p}^f = [p_x^f, p_y^f, p_z^f]$ is the final position, $\mathbf{v}^f = [v_x^f, v_y^f, v_z^f]$ is the final velocity, B^f is the final ballistic coefficient, and σ is the ablation coefficient. We use the end of the observable trajectory in the state estimate as it is far easier to constrain the ballistic coefficient, which relates to meteoroid mass, to be greater than zero for all times along the observable trajectory ($B(t) > 0$). These first eight parameters are always required to define the trajectory. If one or more fragmentation events are suspected, the percentage fragmentation, δ_{frag} , and the time of fragmentation, t_{frag} , are added to the state for every suspected fragmentation event. If any observatories are found to contain timing offsets, an estimated offset time, Δt , is added to the state for every offset observatory. Finally, if one or more observatories contain lines of sight without relative times, an estimated relative time, t^{rel} , is added for every line of sight that is missing timing information.

To calculate these estimates, we must first get an idea of the trajectory from simpler triangulation methods. Using a bootstrapping approach, we can build up from the MOP (Ceplecha 1987) to the SLLS (Borovicka 1990), from which we can then estimate most of the state parameters. The time components are estimated first to ensure we calculate the correct position, velocity, and ballistic coefficient parameters.

To determine if any observatories have a timing offset problem, we start by assuming that all of the sensors are offset and determine what Δt is needed to synchronize them. This involves first designating a “master” observatory to act as a temporal anchor, chosen as the observatory with the most lines of sight with timing. Next, we adjust the estimated timing offsets for every other observatory to minimize the differences in lengths along the SLLS line when compared to the “master,” interpolating if necessary. If the estimated offset is greater than a given tolerance, say 0.05 s, then the timing from that observatory is used as relative timing only, and the estimated offset is added to the state to be optimized.

⁶ For online access to the source code of the DTF algorithm, please follow this link: https://github.com/desertfireballnetwork/dfc_triangulation/.

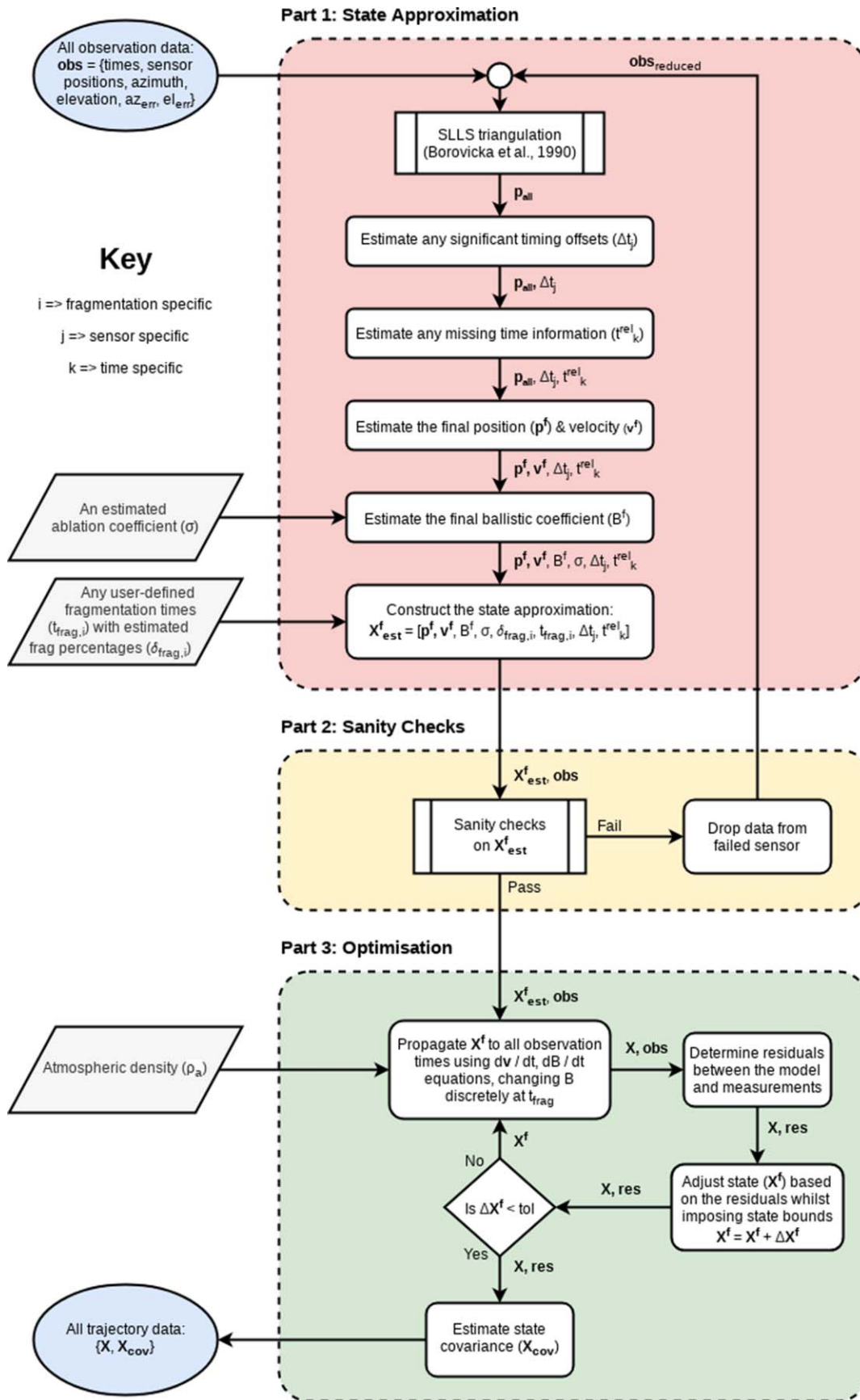


Figure 1. A pseudocode flowchart of the DTF algorithm divided into its three main parts: state approximation (red), sanity checks (yellow), and optimization (green). The start and end of the algorithm are highlighted in blue, and all other inputs are highlighted in gray.

Table 1

State Boundary Conditions Given to the Least-squares Algorithm to Ensure Realistic Results, where LB and UB Stand for Lower Bound and Upper Bound, Respectively

State Parameters	p^f (km)	v^f (km s ⁻¹)	B (kg m ⁻²)	σ (kg J ⁻¹)	δ_{frag} (%)	t_{frag} (s)	$\Delta t, t^{\text{rel}}$ (s)
LB	* - 40	* - 5	10 ⁻¹⁰	3 × 10 ⁻⁹	0	t_{min}	* - 10
UB	* + 40	* + 5	10 ⁴	3 × 10 ⁻⁶	100	t_{max}	* + 10

Note. Also, the star symbol represents the associated estimated state parameter as determined in Part 1.

All of the lines of sight without timing are then very roughly estimated by comparing their lengths along the SLLS line to a modeled length/time function. This function is constructed by fitting a trajectory of constant velocity to the SLLS lengths along the line over time. All timeless lines of sight have their along-track lengths converted to relative timing, t^{rel} , and are subsequently added to the state estimate to be optimized. After optimization, these lines of sight each produce a zero along-track error, as expected.

Now, using the rough timing corrections above, we are able to more accurately estimate the meteoroid’s final position and velocity from the SLLS fit. Put simply, the estimated position is merely the final triangulated point along the SLLS line, and the estimated velocity is a least-squares average velocity of the last eight SLLS triangulated positions. The ablation coefficient, σ , is initially estimated as $14 \times 10^{-9} \text{ s}^2 \text{ m}^{-2}$ in all cases (Sansom et al. 2015). The ballistic coefficient, B^f , is roughly determined by adjusting it to equate the SLLS trajectory length with the propagated trajectory length using the meteoroid’s dynamic equations of motion—Equations (3) and (4). This is achieved using Brent’s root-finding method on the range $\log_{10}(B^f) \in [1, 4]$, which approximately equates to a meteoroid mass range of 0.1 g–100 ton sphere of chondritic density (3500 kg m⁻³).

If any fragmentation is suspected by the user, one or more fragmentation times are able to be input to the algorithm and serve as the t_{frag} parameter in the state estimate. The fragmentation percent, δ_{frag} , is always estimated initially as 30% and adjusted upon optimization.

We must note that these estimates’ sole purpose is to start the optimization sufficiently close to the global minimum to allow convergence. Once the minimization algorithm begins, the measurements are the only things directly influencing the trajectory solution; it is not building off already processed data.

Part 2: Sanity Checks. As some fireball data reduction pipelines can be almost completely automated, such as those of the GFO, there is a chance sensor data are corrupt or have been incorrectly grouped. This could occur for a variety of reasons, including calibration errors, planes and/or satellites being misidentified as meteoroids, or the rare cases where multiple simultaneous fireballs are incorrectly correlated across sensors.

To avoid triangulation errors within the optimization routine, a variety of sanity checks need to be performed to remove erroneous data before optimization is attempted. All of the following checks use the rough triangulation of SLLS and the state approximation (as determined in Part 1) to ensure that each observatory’s triangulated observations:

1. Decrease in height over time.
2. Change in height at roughly the same rate.
3. Produce sufficiently low SLLS residuals.
4. Triangulate to positions above the ground.
5. Triangulate to positions less than 200 km altitude.

6. Produce a final state velocity estimate less than 200 km s⁻¹.

These conditions are designed to be quite extreme to prevent accidentally discarding any valid data that have happened to triangulate poorly using the SLLS procedure. If any data are found inaccurate, the first sensor to fail a condition above is eliminated, and the procedure begins over from the state approximation (Part 1).

Part 3: Optimization. Now that we have an initial state estimate (Part 1) using good data (Part 2), we are in a position to begin the trajectory optimization. This step could be performed with any robust minimization routine that imposes bounds on the optimized state to ensure realistic results. For reliability, we have elected to use SciPy’s built-in least-squares function, which has been thoroughly tried and tested (Virtanen et al. 2020). Within this function, the trust region reflective (TRF) method is chosen as it is robust and permits bounds to be set on the allowable state. We define rather generous state bounds to give the optimization routine enough room to effectively search the state space while at the same time keeping the resulting state physically realistic; see Table 1.

The chosen TRF method also offers the option for user-defined Jacobian and state step size. For accuracy and computational speed, we provide a parallelized custom Jacobian function that utilizes a central differencing routine. The step size is defined equal to the change in state used in the Jacobian’s central differencing algorithm to avoid state divergence by overshooting the bounds of Jacobian linearity.

Once the least-squares algorithm is set up and initiated, the state is propagated to all other observation times using Equations (3) and (4) combined with an ordinary differential equation solver, such as SciPy’s odeint function (Virtanen et al. 2020). These observation times are possibly adjusted by an offset, Δt_j , or completely generated, t_k^{rel} , using the parameters within the current state estimate (Equation (5)). Also, if any fragmentation parameters exist within the to-be-optimized state (Equation (5)), the state propagation procedure is interrupted at these specified fragmentation times, $t_{\text{frag},i}$, to discretely change the meteoroid’s mass by a specified percentage, $\delta_{\text{frag},i}$, while keeping all other state parameters the same to ensure trajectory continuity.

The positions within the set of propagated states are subsequently converted to lines of sight given the various observatory’s locations and times. These predicted lines of sight are differenced from the observed lines of sight to give the angular along-track and cross-track residual components. With the help of the Jacobian to show the direction of the local (and hopefully global) minimum, the state parameters are adjusted to minimize these angular residuals, weighted by their individual astrometric uncertainties. This procedure occurs iteratively until the state does not differ significantly enough from one iteration to the next, therefore signifying that a minimum is

reached and the resulting state matches the observations as closely as possible.

Now that the optimized state solution is obtained, the state errors are determined (as discussed in Section 2.2) and propagated to all of the other observation times alongside the state itself before being saved to file for subsequent orbit determination and possible dark-flight analysis. Various plots are then constructed using these data; see Section 3.2.

2.2. Notes on Errors

We must note that the least-squares algorithm used within the DTF method does not produce errors. Instead, covariance errors can be estimated afterward from both the Jacobian of the optimized state and the covariance on the line-of-sight measurements as follows (Bevington et al. 1993):

$$\chi_{\text{cov}} = \chi_{\text{cov}}^{\text{res}} + \chi_{\text{cov}}^z, \quad (6)$$

$$\chi_{\text{cov}}^{\text{res}} = (d\chi/d\text{res})^T \text{diag}(\text{res}^2) (d\chi/d\text{res}), \quad (7)$$

$$\chi_{\text{cov}}^z = (d\chi/d\text{res})^T (\text{dres}/dz)^T z_{\text{cov}} \times (\text{dres}/dz) (d\chi/d\text{res}), \quad (8)$$

$$d\chi/d\text{res} = (\mathbf{J}\mathbf{J}^T)^{-1}\mathbf{J}^T, \quad (9)$$

where \mathbf{J} is the state Jacobian matrix, describing how the residuals change with a change in state; $d\chi/d\text{res}$ is the inverse of the Jacobian, describing how the state changes with a change in residuals; dres/dz is a coordinate transform, describing how the residuals (along-track/cross-track) change with a change in line-of-sight measurements (R.A./decl.); z_{cov} is the covariance on the measurements; and $\text{diag}(\text{res}^2)$ is the residual vector at the optimized state, diagonalized.

As shown in Equation (6), we are able to incorporate the residual covariance due to the spread in residuals around the model, $\chi_{\text{cov}}^{\text{res}}$, and measurement covariance due to the astrometric uncertainty, χ_{cov}^z , into an overall covariance estimate. Separate testing showed that the measurement covariance component accurately reflected the covariance of the state through repeated Monte Carlo analyses in which the measurements were varied within their astrometric covariance space.

However, we must also note that the uncertainty formulation discussed above does not account for errors arising due to the meteoroid equations of motion as well as assumptions made within this model (Equations (3) and (4)), such as a constant ablation coefficient, shape, and density of the meteoroid throughout the visible trajectory. Therefore, the determined covariance from Equation (6) can be viewed as minimum uncertainties given the observations.

3. Results and Discussion

To demonstrate and compare the capabilities of the four previously discussed triangulation methods, we conduct two independent comparative analyses: the first study uses over 100,000 randomly simulated trajectories, comparing the fitted initial velocity vector to the simulated “truth.” The second study uses a real fireball event, captured by multiple observatories within the DFN.

3.1. Randomized Simulations

To fully analyze the accuracy of a triangulation algorithm through the full range of possible trajectory conditions, one must rely on simulations. Simulations allow us to compare a triangulation solution against the unaltered trajectory “truth.” For the following comparative analysis, a fireball simulator was designed, built, and heavily tested under a variety of initial conditions before being used to compare the various triangulation methods.

This fireball simulator begins with a set of randomized physical and dynamical initial conditions at the top of the atmosphere, completely defining a meteoroid’s state at that point. This randomized state is then numerically propagated forward in time using the meteoroid’s 3D differential equations of motion until the meteoroid’s speed relative to the ground falls below 2 km s^{-1} or it completely ablates ($B \rightarrow 0$), whichever occurs first. Likewise, the initial meteoroid’s state is also propagated back in time until the meteoroid’s height exceeds 200 km. These propagation bounds are chosen to confidently cover the meteoroid’s luminous phase of its trajectory.

Once this extended simulated trajectory has been established, perfect azimuth and elevation measurements are generated every 0.1 s for two randomized observatory locations. These simulated measurements are then uniquely pruned for each sensor depending on their calculated visibility—i.e., while the meteoroid is more than 10° above the horizon and ablating rapidly enough to be detectable from each observatory’s perspective (Ceplecha et al. 1996; Sansom et al. 2019). The resulting measurements are then varied within some randomized Gaussian measurement error to better reflect reality.⁷

The initial state of these simulated trajectories was generated with a fixed latitude of 0° , a fixed longitude of 0° , a fixed height of 100 km, a uniformly random slope between 10° and 90° from local horizontal (avoids potential skipping events), a uniformly random bearing between 0° and 360° , and a uniformly random speed between 12 and 72 km s^{-1} (produces only heliocentric orbits). Additionally, the meteoroid was initialized with a fixed density of 3500 kg m^{-3} (rough ordinary chondrite meteorite density), a fixed spherical shape, a fixed ablation coefficient of $10^{-8} \text{ kg J}^{-1}$ (using Table 2 of Sansom et al. 2015 as a guide), and a uniformly random mass in log space between 100 g and 100 kg (typical fireball events). Two uniformly random observatory locations that could view the center of the observable trajectory at an elevation greater than 20° were generated. This did not always generate geometrically favorable observation combinations.

The simulated line-of-sight observations were given a measurement error of 2/4, characteristic of the measurement errors given by a DFN observatory (Howie et al. 2017a). Gural (2012) found that the resulting radiant error was proportional to the measurement error, and therefore, any results found through this analysis can be linearly extrapolated to imaging systems of higher or lower resolution.

In this analysis, we generated 123,337 sets of realistic double-station measurements from random trajectories using the fireball simulator. Each measurement set was subsequently passed to the four triangulation methods for trajectory fitting:

⁷ This trajectory can also be affected by multiple randomized or user-defined fragmentation events, and/or systematic observatory timing offsets to increase realism; however, these abilities are not used in this analysis.

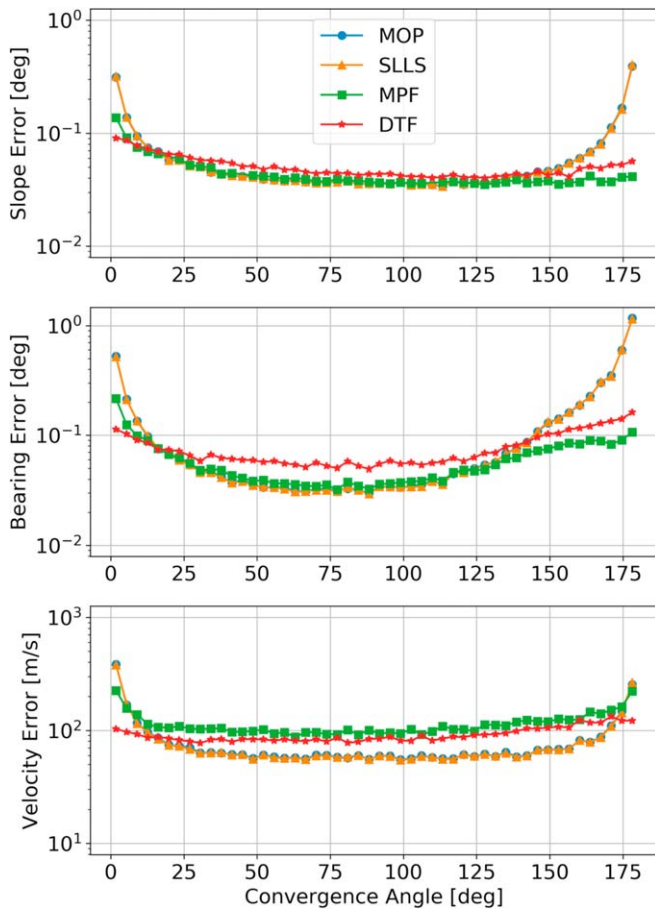


Figure 2. The median absolute differences between the simulated and fitted radiant at the top of the meteoroid’s trajectory by varying the observation convergence angle.

the MOP, the SLLS method, the MPF⁸ method, and the novel DTF method. The original simulated radiant velocity vector and the four fitted radiant velocity vectors from the top of the trajectory are then compared, distinguishing the differences in slope, bearing, and velocity magnitude components.

Similar to the analysis performed by Gural (2012), the difference between the true and estimated radiant parameters are statistically analyzed by considering its median value within small, equally divided bins that subtend the x -axis. This avoids excess clutter and highlights the general trends of the various triangulation methods.

Using the approach described above, we can compare the fitting errors against different meteoroid trajectory parameters, such as the observation convergence angle, initial speed, trajectory duration, and trajectory length as shown in Figures 2–5, respectively.

From these simulation results, we notice that all triangulation methods generally agree and tend to follow the same trends—especially between the MOP and SLLS approaches. Areas with the most model inaccuracy arise when a meteoroid trajectory is viewed from observatories of low convergence angle, is short in length, or displays a relatively slow entry velocity. Interestingly, these are the

⁸ Gural (2012, p. 1411) states that “the algorithm is not ill-conditioned to having too many velocity fitting parameters as long as there is measurement sample support.” Therefore, we have chosen to use the exponentially dependent deceleration model specified in Equation (4) of Gural (2012) for MPF analysis within this paper.

regions that the DTF method either matches or exceeds in accuracy when compared to the alternative triangulation methods. In particular, the DTF provides a more accurate trajectory solution at low convergence angles ($<10^\circ$), slow to moderate entry velocities ($<25 \text{ km s}^{-1}$), and extremely fast entry velocities ($>65 \text{ km s}^{-1}$).

Regions where the DTF method appears to perform poorly could be due to the underlying least-squares algorithm either reaching a nonglobal minimum or simply terminating optimization procedures too early. Regardless, the estimated errors calculated as part of the DTF procedure (Section 2.2) are on the same order as the median absolute deviations shown from these simulations. This indicates that the true meteoroid trajectory is accurately encompassed within the DTF errors, which is the ultimate goal of meteoroid trajectory modeling.

It is also interesting to note that in most trajectory scenarios, the modeled velocity error is on the order of 0.1 km s^{-1} . However, as stated before in Gural (2012), the magnitude of this model error is directly proportional to the uncertainty in the line-of-sight observations. Therefore, we can conclude that meteoroid events with observation errors less than the 2’/4 simulated here should result in a velocity accuracy better than $\sim 0.1 \text{ km s}^{-1}$ —the threshold needed for accurate identification of meteoroid source regions within the solar system (Granvik & Brown 2018).

Although extensive simulations of meteoroid trajectories observed through two sensors were used to statistically analyze and compare the different triangulation methods, analysis of meteoroid trajectories observed by more than two sensors was not explored here. It would be insightful, however, to perform a similar statistical analysis on cases with three or more sensors. In general, trajectory results from all triangulation methods would improve in accuracy given additional sensor data—not just due to an increase in data density, but also due to the additional triangulation information an extra sensor can provide. To what degree is yet to be shown and will be the subject of future work.

3.2. Case Study: Fragmentation Event (DN141125_01)

Simulations are a way to thoroughly investigate and compare various models to an estimated reality. However, no simulation can 100% replicate reality. It is for this reason that we analyze and compare the various meteoroid triangulation methods using a real-world example. We choose an event with visible signs of fragmentation to highlight the fragmentation handling within the DTF method, as shown in Figure 6.

This fireball event with visible fragmentation, referred to as DN141125_01, was captured by five DFN observatories—two of which could not be resolved for timing due to the distance of the observations. Although the DTF method can incorporate data with this lack of timing information, we chose to discard the data from these observatories for triangulation comparison purposes. The DN14125_01 event was visible for 9.24 s, comprising 459 line-of-sight observations at a maximum convergence angle of 35° . The triangulation for event DN141125_01 is shown visually in Figure 7 and is summarized in Table 2.

To determine which triangulation model best fits the line-of-sight observations, we compare the residual magnitudes as stated in Table 2 and shown more thoroughly in Figure 8. Unsurprisingly, the residuals in the cross-track direction are smallest using the SLLS method as this is its optimization

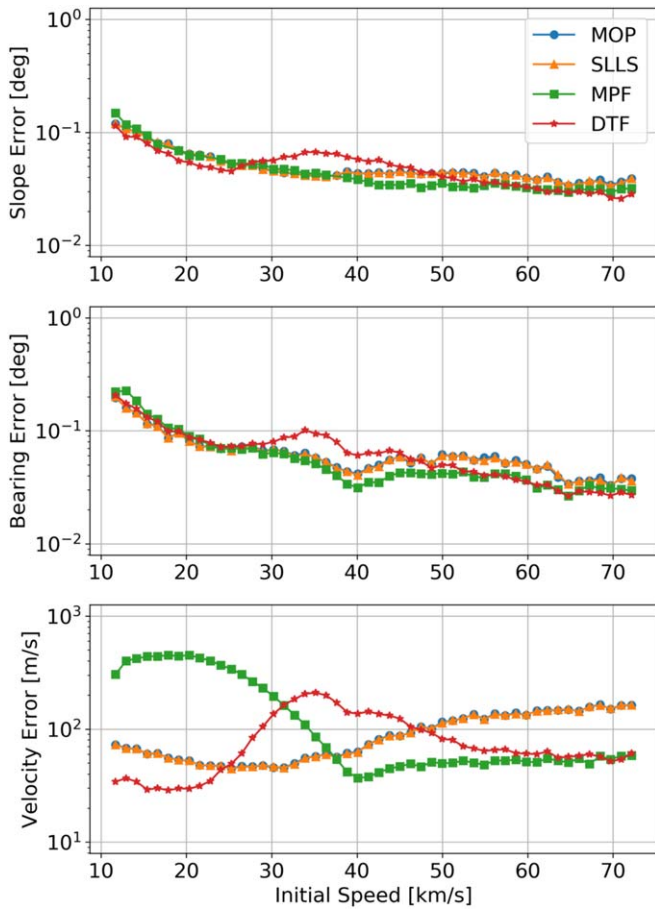


Figure 3. The median absolute differences between the simulated and fitted radiant at the top of the meteoroid’s trajectory by varying the initial speed.

parameter. However, the DTF_{frag} model possesses the smallest total residuals.

The velocities determined by the various triangulation methods rely on different models, each containing unique assumptions. The velocity determination algorithm used within the MOP and SLLS methods fits the 1D meteoroid equations of motion to the lengths along the 1D trajectory, assuming an exponential atmosphere (Pecina & Ceplecha 1983). The velocity calculated by the MPF method uses a purely empirical formula (Whipple & Jachia 1957; Gural 2012). Lastly, the velocity results from the DTF method consults the meteoroid’s 3D equations of motion directly, without any simplifying straight-line or atmospheric assumptions. The subtleties between these velocity models using data from event DN141125_01 are compared in Figure 9.

As shown in Table 2 and Figure 9, the final velocity predicted by the MPF method does not appear to follow the instantaneous velocity scatter, suggesting the exponentially dependent velocity model does not reflect reality for long fireball-type events. Excluding the MPF velocity, the remaining velocity models seem very similar, varying by about 300 m s^{-1} at the extremities. However, this 300 m s^{-1} variation would still lead to considerably different dark-flight and orbit regression results.

As discussed in Section 2, the DTF method is able to resolve the meteoroid’s ballistic coefficient over time, $B(t)$. By assuming a constant meteoroid shape and density, we can estimate the meteoroid’s mass throughout the observed luminous trajectory directly using the line-of-sight observations—unlike any other compared triangulation method. This feature not only helps

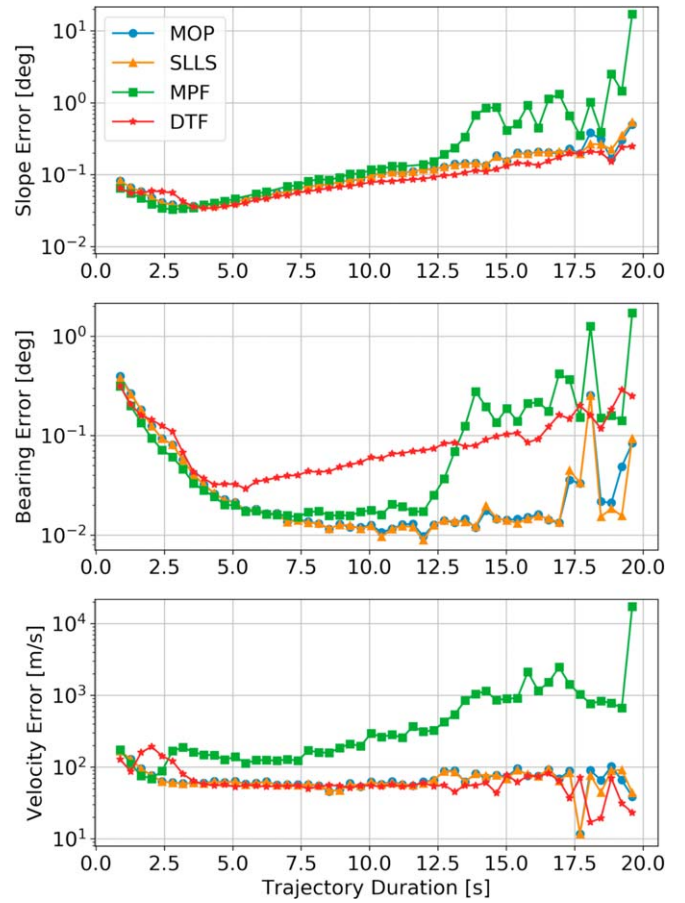


Figure 4. The median absolute differences between the simulated and fitted radiant at the top of the meteoroid’s trajectory by varying the trajectory duration, where duration is roughly proportional to the number of collected observations.

diagnose meteorite-dropping events but assists greatly in constraining the meteorite search area. The mass estimates for event DN141125_01 using the DTF and DTF_{frag} methods are compared in Figure 10. The DTF_{frag} method predicts the meteoroid from DN141125_01 broke up around 5.3 s, at an altitude of 47.3 km—consistent with the visible fragmentation shown in Figure 6.

To summarize this comparison of triangulation methods, the DTF with fragmentation handling (DTF_{frag}) appears to be the best model for event DN141125_01. While there may be events that are better suited to the other triangulation methods, the simulations discussed in Section 3.1 show that the DTF method is an equal if not better choice for most events. Additionally, the DTF method can estimate the mass of the meteoroid from the line-of-sight observations directly, as discussed in Sections 1.1–1.3.

4. Future Functionality

While the proposed DTF method appears successful in its current form and poses considerable merit, there are a few improvements that could be applied to increase realism and draw out additional subtleties within the gathered data. These improvements include:

Remove model assumptions. In the derivation of the meteoroid’s equations of motion (Equations (3) and (4)), the meteoroid is assumed to be spinning rapidly enough to uniformly ablate

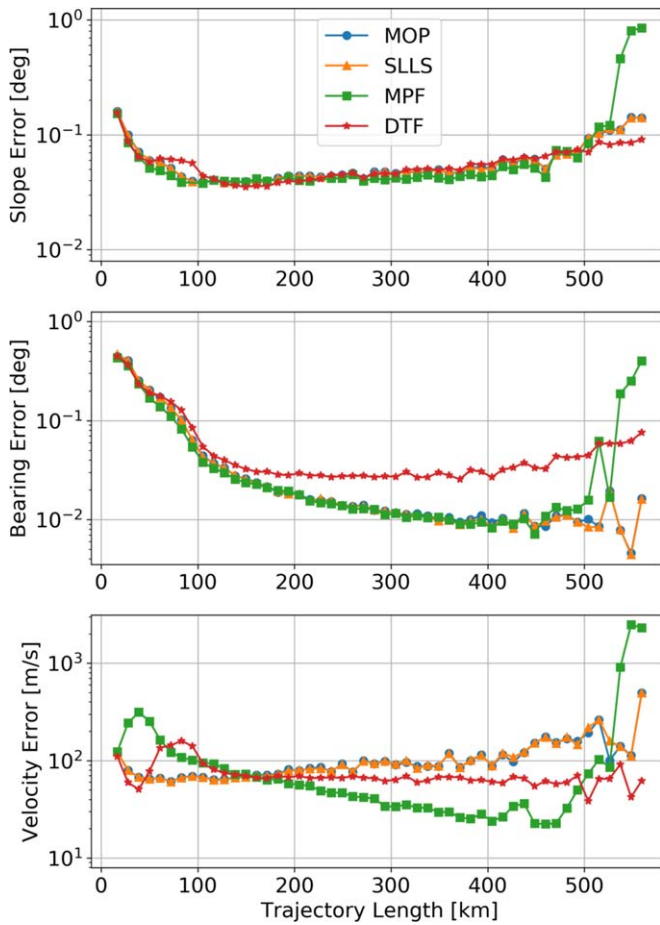


Figure 5. The median absolute differences between the simulated and fitted radiant at the top of the meteoroid’s trajectory by varying the trajectory length, where length can be roughly related to initial speed and trajectory duration.

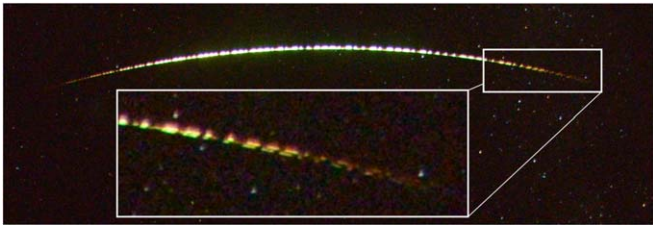


Figure 6. The captured long-exposure image of event DN141125_01 taken from the Mulgathing station within the Desert Fireball Network, showing visible signs of fragmentation toward the end of the luminous trajectory.

over its surface ($\mu = 2/3$) and have a constant drag coefficient, shape, and density throughout the luminous portion of its trajectory. While Bouquet et al. (2014) show these assumptions are reasonable and often used in meteor physics, removing as many of them as possible would lead to a more realistic meteoroid model, and therefore more accurate meteoroid orbit and impact location predictions.

Light-curve incorporation. With the inclusion of light-curve data, we would have the opportunity to better model meteoroid mass loss along the trajectory, which would act to further constrain the meteoroid state and its associated uncertainty. Luminous efficiency models, such as that by Gritsevich & Koschny (2011), might be relatively easily incorporated into the state propagation of the meteoroid to better estimate its physical and dynamical parameters.

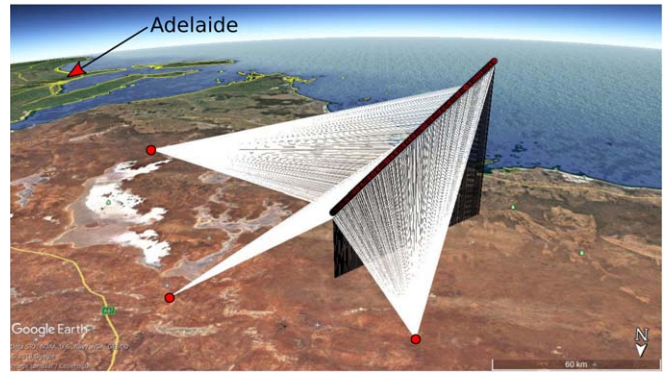


Figure 7. The triangulation of event DN141125_01 using a total of 459 line-of-sight measurements from three South Australian observatories within the Desert Fireball Network: Mulgathing, Northwell, and Mount Ives.

Table 2

Summary of Event DN141125_01 Trajectory Parameters Using the Four Triangulation Methods Discussed in This Paper: The Method of Planes (MOP), the Straight-line Least Squares (SLLS), the Multiparameter Fit (MPF), and the Dynamic Trajectory Fit (DTF)

	MOP	SLLS	MPF	DTF	DTF _{frag}
Along-track residuals (′)	8.700	4.099	6.385	2.543	2.332
Cross-track residuals (′)	2.427	0.861	2.314	3.392	3.411
Total residuals (′)	9.033	4.188	6.792	4.240	4.132
R.A. (°)	345.245	345.089	345.088	345.014	345.010
Decl. (°)	−46.351	−46.655	−46.663	−46.333	−46.311
Latitude ₀ (°)	−31.593	−31.600	−31.600	−31.593	−31.592
Longitude ₀ (°)	133.770	133.767	133.765	133.768	133.769
Height ₀ (km)	80.441	80.752	80.815	80.285	80.189
Velocity ₀ (km s ^{−1})	13.977	14.095	14.381	13.989	13.908
Slope ₀ (°)	27.247	27.238	27.236	27.091	27.082
Azimuth ₀ (°)	49.004	48.656	48.656	48.962	48.977
Mass ₀ (kg)	N/A	N/A	N/A	0.901	1.605
Latitude _f (°)	−31.011	−31.011	−31.012	−31.010	−31.010
Longitude _f (°)	134.545	134.541	134.538	134.539	134.540
Height _f (km)	30.456	30.627	30.732	30.543	30.521
Velocity _f (km s ^{−1})	4.711	4.954	3.041	4.738	4.892
Slope _f (°)	26.368	26.353	26.352	26.484	26.476
Azimuth _f (°)	48.602	48.253	48.254	48.178	48.194
Mass _f (kg)	N/A	N/A	N/A	0.081	0.113

Note. In addition, the triangulation solution of the dynamic trajectory fit with fragmentation (DTF_{frag}) was also given to highlight this added fitting feature. The results are divided into four sections; the standard deviations of the trajectory residuals to indicate the goodness of fit, the radiant direction for possible meteor stream classification, the initial trajectory position and velocity at 15:21:15.386 UTC used for orbit determination, and the final trajectory position and velocity at 15:21:24.626 UTC used for dark-flight analysis. DN141125_01 had a maximum observed convergence angle of 35°.

Automated fragmentation determination. Currently, we rely on a user-defined time of fragmentation. However, with full light-curve history, we should be able to flag fragmentation events from light-curve peaks alone, therefore negating any user-required input to the algorithm. However, this functionality could easily be integrated upstream in a larger data reduction pipeline using measurements from highly sensitive radiometers (Buchan et al. 2019), not necessarily integrated into the triangulation method itself.

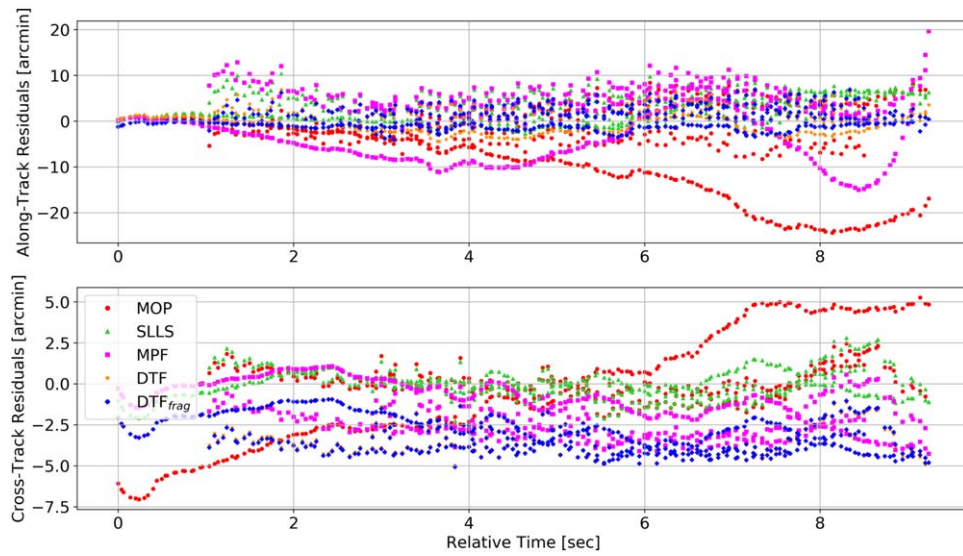


Figure 8. The along-track and cross-track residuals from all three observatories of the DN141125_01 event using five triangulation methods: the four discussed methods as well as the dynamic trajectory fit method with fitted fragmentation (DTF_{frag}). The standard deviation of these residuals are given in Table 2.

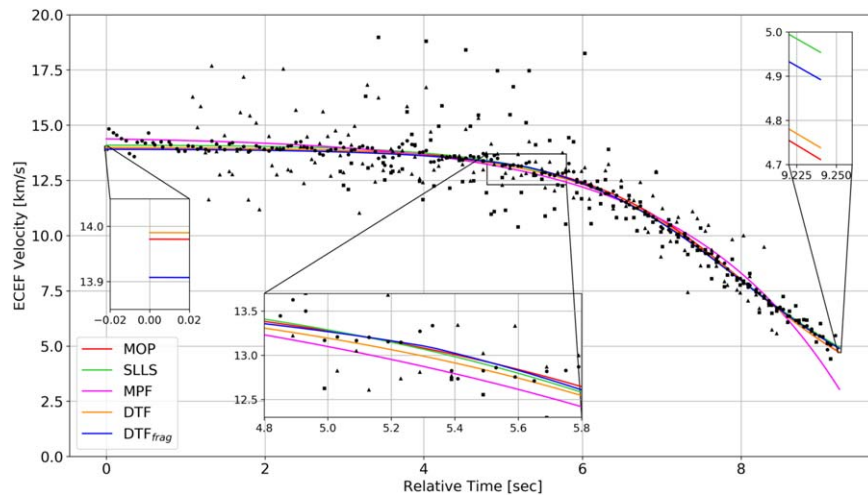


Figure 9. The modeled velocity of the DN142511_01 event from the various triangulation methods, as discussed in Sections 1 and 2. The surrounding scatter is the instantaneous velocities as calculated by the change in adjacent SLLS positions along the trajectory over the change in time from each observatory, separately. Velocity subtleties at the beginning, middle, and end of the trajectory are highlighted by the zoomed-in sections.

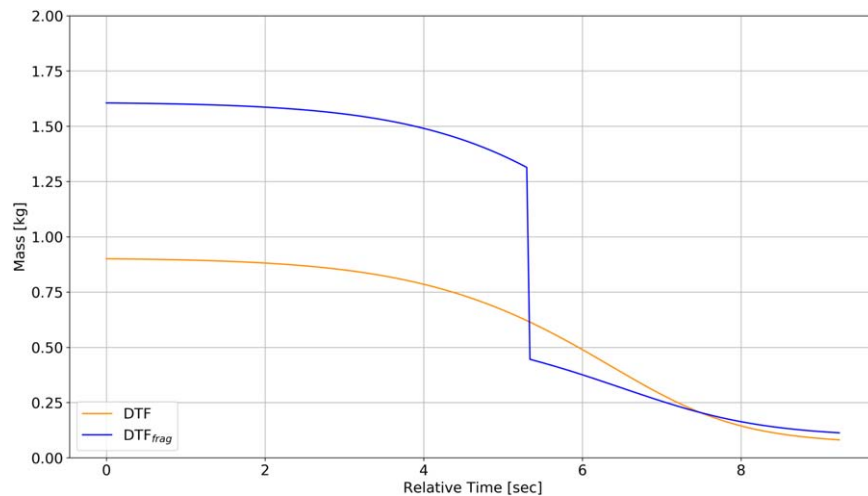


Figure 10. The estimated mass of the DN141125_01 event throughout its trajectory determined by the dynamic trajectory fit, both with (DTF) and without (DTF_{frag}) fragmentation fitting. The other three triangulation models are not plotted here as they do not produce mass estimates.

Meteoroid spin modeling. For some particularly long fireballs, such as Case 1 of Sansom et al. (2019), trajectories appear to considerably deviate from the fall plane, suggesting there are unaccounted aerodynamic effects. We hypothesize this might be in part due to the Magnus effect at high velocities, that is, the resulting curvature of an object's trajectory due to its spin. It would be very interesting to model these cases with meteoroid spin considered. The proposed DTF method would simply require an additional three state parameters to model this phenomenon, namely the angular velocity vector, $\omega_{\text{spin}} = [\omega_x, \omega_y, \omega_z]$. It would be conceivable to extend the DTF method to optimize without spin, only reoptimizing with spin if the measurements did not adequately match the model (reduced chi-squared $\chi_r^2 \approx 1$).

Global triangulation solution. Until alterations to the DTF algorithm are made to avoid some of the discussed inaccuracies (see Section 3.1), the alternative triangulation methods could be utilized under certain trajectory conditions—for example, using SLLS/MPF methods for those meteoroid cases with determined velocities between 25 and 65 km s⁻¹. Alternatively, one could even perform all triangulation methods on the same event and combine their results with various weights depending on the meteoroid's determined traits, such as speed and convergence angle.

5. Conclusions

Meteoroid orbits and meteorite samples provide invaluable information that helps planetary scientists investigate solar system formation and the origin of life on Earth. Fireball networks around the globe are on the forefront of providing this knowledge. However, the accuracy of the determined orbit and the chance of meteorite recovery both rely heavily on the accuracy of the underlying meteoroid triangulation method.

Three triangulation methods have been proposed in the past: the MOP (Ceplecha 1987), the SLLS method (Borovicka 1990), and the MPF (Gural 2012). The first two listed methods above separate out the geometric fit from the dynamic modeling. In 2012, Gural simplified this procedure to a single step, changing the well-known convergence angle from that between planes to that between simultaneous rays—a clear advantage over the past traditional triangulation methods. However, the velocity models suggested within Gural (2012) are empirically derived for small meteors and do not reflect reality, particularly for meteorite-dropping events. The proposed novel DTF method not only contains a more realistic dynamic model, but it possesses the ability to determine the meteoroid's ballistic coefficient throughout the observable trajectory directly from the line-of-sight measurements, unlike any other proposed triangulation method. With meteoroid shape and density assumptions, this ballistic coefficient can be easily translated into meteoroid mass.

Over 100,000 multistation meteoroid simulations revealed the advantage of the DTF method particularly for relatively slow entry events (<25 km s⁻¹) as well as events observed from low convergence angles (<10°). Additionally, a visibly fragmenting fireball event captured by three stations of the DFN was used to compare the four triangulation methods. The DTF with fragmentation was shown to best match the observations, with the predicted fragmentation time in agreement with the observed data.

The method proposed here could be easily modified to fit arbitrarily complex equations of motion, to include light-curve data, and to provide automated fragmentation detection in the future.

We would like to thank the reviewer, Maria Gritsevich, whose comments and suggestions helped to improve and clarify this manuscript. This work was funded by the Australian Research Council as part of the Australian Discovery Project scheme and supported by resources provided by the Pawsey Supercomputing Centre with funding from the Australian Government and the Government of Western Australia. This work was also supported by an Australian Government Research Training Program (RTP) Scholarship.

This research made use of Astropy, a community-developed core Python package for Astronomy (Astropy Collaboration et al. 2013). Additionally, the majority of figures were generated using Matplotlib, another community-developed Python package (Hunter 2007).

ORCID iDs

Trent Jansen-Sturgeon  <https://orcid.org/0000-0002-0363-0927>
 Eleanor K. Sansom  <https://orcid.org/0000-0003-2702-673X>
 Hadrien A. R. Devillepoix  <https://orcid.org/0000-0001-9226-1870>
 Philip A. Bland  <https://orcid.org/0000-0002-4681-7898>
 Martin C. Towner  <https://orcid.org/000-0002-8240-4150>
 Robert M. Howie  <https://orcid.org/0000-0002-5864-105X>
 Benjamin A. D. Hartig  <https://orcid.org/0000-0002-8646-0635>

References

- Astropy Collaboration, Robitaille, T. P., Tollerud, E. J., et al. 2013, *A&A*, **558**, A33
 Bevington, P. R., Robinson, D. K., Blair, J. M., Mallinckrodt, A. J., & McKay, S. 1993, *ComPh*, **7**, 415
 Borovicka, J. 1990, *BAICz*, **41**, 391
 Bouquet, A., Baratoux, D., Vaubaillon, J., et al. 2014, *P&SS*, **103**, 238
 Bronshten, V. A. 1983, *Physics of Meteoric Phenomena* (Dordrecht: Reidel)
 Buchan, S. R. G., Howie, R. M., Paxman, J., & Devillepoix, H. A. R. 2019, arXiv:1907.12807
 Ceplecha, Z. 1961, *BAICz*, **12**, 21
 Ceplecha, Z. 1987, *BAICz*, **38**, 222
 Ceplecha, Z., Spalding, R. E., Jacobs, C. F., & Tagliaferri, E. 1996, *Proc. SPIE*, **2813**, 46
 Granvik, M., & Brown, P. 2018, *Icar*, **311**, 271
 Gritsevich, M., & Koschny, D. 2011, *Icar*, **212**, 877
 Gritsevich, M. I. 2009, *AdSpR*, **44**, 323
 Gural, P. S. 2012, *M&PS*, **47**, 1405
 Howie, R. M., Paxman, J., Bland, P. A., et al. 2017a, *ExA*, **43**, 237
 Howie, R. M., Paxman, J., Bland, P. A., et al. 2017b, *M&PS*, **52**, 1669
 Hunter, J. D. 2007, *CSE*, **9**, 90
 Jacchia, L., Verniani, F., & Briggs, R. E. 1967, *SCoA*, **10**, 1
 Jenniskens, P. 2006, in *Proc. Int. Meteor. Conf.*, ed. F. Bettonvil & J. Kac (Cambridge: Cambridge Univ. Press), 56
 Pecina, P., & Ceplecha, Z. 1983, *BAICz*, **34**, 102
 Pecina, P., & Ceplecha, Z. 1984, *BAICz*, **35**, 120
 Picone, J. M., Hedin, A. E., Drob, D. P., & Aikin, A. C. 2002, *JGRA*, **107**, 1468
 Sansom, E. K., Bland, P., Paxman, J., & Towner, M. 2015, *M&PS*, **50**, 1423
 Sansom, E. K., Jansen-Sturgeon, T., Rutten, M. G., et al. 2019, *Icar*, **321**, 388
 Virtanen, P., Gommers, R., Oliphant, T. E., et al. 2020, *NatMe*, **17**, 261
 Whipple, F. L., & Jacchia, L. G. 1957, *SCoA*, **1**, 183